ELSEVIER

Coordination Chemistry Reviews
219–221 (2001) 573–604

COORDINATION CHEMISTRY REVIEWS

www.elsevier.com/locate/ccr

New experimental techniques for magnetic anisotropy in molecular materials

Andrea Cornia [a], Dante Gatteschi [b,*], Roberta Sessoli [b]

[a] *Department of Chemistry, University of Modena and Reggio Emilia, via G. Campi 183, Modena, Italy*

[b] *Department of Chemistry, University of Florence, via Maragliano 77, 50144 Florence, Italy*

Received 14 September 2000; accepted 27 January 2001

Contents

* Corresponding author. Tel.: +39-55-3216324; fax: +39-55-354845.
E-mail address: gattesch@chim1.unifi.it (D. Gatteschi).

PII: S0010-8545(01)00352-6

Abstract

Magnetic anisotropy is a very important property in magnetochemistry. Its knowledge allows us to obtain a fundamental understanding of the electronic structure of both simple paramagnetic species and of magnetically coupled systems. The difficulties associated with its experimental determination have so far limited its investigation. Recently new experimental techniques using superconducting quantum interference devices (SQUID) and micro-SQUID arrays as well as cantilever torque magnetometry have drastically reduced the size of the crystals needed for the measurements, thus opening new perspectives. We will briefly review here these techniques, with the aim to advertise their use in the chemical community.

Keywords: Magnetic anisotropy; Micro-SQUID arrays; Torque magnetometry; Molecular magnetism

1. Introduction

Magnetochemistry is that part of chemistry which describes the magnetic properties of compounds and uses magnetic techniques for obtaining structure and bonding information [1,2]. The first impetuous development of magnetochemistry was in the 1950s and 1960s, when the availability of semi-quantitative theories, like crystal-field and ligand-field theories, allowed one for the first time to effectively relate the structure of transition-metal complexes with the nature of the chemical bond. The measurement of the effective magnetic moment, $\mu_{\text{eff}} = \sqrt{8\chi T}$, at room temperature provided an indication of the number of unpaired electrons present in the metal center, and allowed one to discriminate, for instance, between high- and low-spin forms of the same metal ion. The temperature dependence of the magnetic susceptibility initially was not of large importance, except when marked differences from the spin-only value were observed, as in the abnormal value seen for copper(II) acetate [3]. In this case measurements down to liquid nitrogen temperature were in general performed.

Another aspect which started to attract attention was that of magnetic anisotropy, when the interest shifted from the high-symmetry model compounds to low symmetry, real-life complexes. In order to acquire a detailed knowledge of the energies of the d orbitals, the different magnetic behavior when the external magnetic field was parallel to the z, x, and y molecular axes was measured. However this was not an easy task with the low-sensitivity magnetometers available at that time [4,5]. Torque magnetometry (TM) was developed, but its actual use was limited to a few chemistry laboratories, which were interested in the sophisticated characterization of transition-metal complexes, and it never really became popular, mainly due to the experimental and theoretical complications.

From the late 1970s the interest of chemists shifted from the use of magnetic measurements for obtaining information on structure and bonding to the design of new materials with expected magnetic properties [6–10]. There was a shift from classical magnetochemistry to molecular magnetism, meaning the application of the

new supramolecular techniques to make objects with new and interesting magnetic properties. This required a much heavier background in magnetism and the mastering of complex experimental techniques. Thus the use of low temperature, involving liquid helium, and of high-sensitivity apparatus, such as superconducting quantum interference device (SQUID) magnetometers, became routine in many chemical laboratories [11]. At the same time it is also true that techniques which had been largely employed by the physicists and which were never really used by chemists, such as AC susceptibility measurements [12], were rediscovered. All these experimental setups were needed for characterizing low-dimensional and three-dimensional molecular magnetic materials, and again for these compounds anisotropic measurements became important. The properties of bulk magnets, such as for instance the coercive field and therefore their soft rather than hard character, depend on magnetic anisotropy [13]. Designing them requires a critical choice of appropriate building blocks.

The discovery that some polynuclear complexes show slow relaxation of the magnetization at low temperature, with hysteresis effects of molecular origin, has been one of the most recent developments in molecular magnetism [14,15]. These systems have properties which are intermediate between classic magnets and quantum magnets [16,17], and have been used to observe for the first time quantum tunneling of the magnetization [18] and quantum oscillations [19] which had been long looked for. The design and the synthesis of these molecules, which have been called single-molecule magnets (SMM) [20,21] requires a detailed understanding of the exchange interactions, which determine the nature of the ground state, and of the mechanisms responsible for the magnetic anisotropy: the possibility to observe slow relaxation of the magnetization at low temperature is linked to this.

All these developments require the use of more efficient instrumentation, which can drastically expand the potentialities of insight into the magnetic properties of molecular materials.

In particular, sensitive instrumentation is needed in order to characterize the very small crystals which are usually obtained for molecular magnets. We wish to review here the techniques used in molecular magnetism for anisotropic magnetic measurements. We will start from SQUID magnetometry, which is now almost a routine in many chemical laboratories. We will not attempt any detailed coverage, but will only show some significant examples. Later we will show the information which can be obtained from two different relatively new experimental techniques, namely cantilever torque magnetometry (CTM) and micro-SQUID (μ-SQUID) arrays, which have been developed in physics laboratories, but are finding interesting applications in molecular magnets.

The organization of the paper will be as follows: we will first recall the foundations of the origin of magnetic anisotropy in molecular clusters, then we will relate the crystal and molecular anisotropies. The following sections will be devoted to the coverage of SQUID magnetometry, high-field CTM and μ-SQUID techniques. A final section will be devoted to conclusions and perspectives.

2. The origin of magnetic anisotropy in molecular clusters

2.1. Single-spin anisotropy

The first component to be considered for the magnetic anisotropy is that associated with the paramagnetic building block which has been chosen for assembling the molecular magnet, be it a SMM or a bulk material. The first idea to develop is that if the system is to show anisotropy it is necessary that there is a difference between the x, say, and the z axis. This can occur if an orbital contribution is present in the ground state. In fact the electron spin by itself has spherical symmetry, and cannot distinguish different molecular axes. If we assume that the individual magnetic center has an orbitally non-degenerate ground state, then the origin of the anisotropy is the admixture of excited states through spin–orbit coupling (SOC) [2]. The assumption of an orbitally non-degenerate ground state is a sound one, because if the system has orbital degeneracy the Jahn–Teller distortion will remove it. Since organic radicals have small SOC constants their magnetic anisotropy is usually very small. In fact the fully organic molecular magnets reported so far have very small coercive fields [9,22]. Matters are different if transition-metal ions, or rare-earth ions, are taken into consideration, because in this case the SOC is large enough to give large anisotropy effects. The SOC can introduce anisotropy both in the way the center responds to an external field (Zeeman effect) and by making some directions preferable even in the absence of an external field (zero-field splitting). The former effect is described by the **g**-tensor in the Zeeman Hamiltonian:

$$\mathbf{H} = \mu_B \mathbf{S} \cdot \mathbf{g} \cdot \mathbf{B} \tag{1}$$

In order to observe g-anisotropy the symmetry of the center must be lower than cubic. If we consider for instance the typical g-values for tetragonally elongated or compressed ions of the first transition series we see that the anisotropy introduced by this term is generally small, except for the ions which have an orbitally degenerate ground state of the T-type. In ions with an orbital-doublet (E) ground state (high-spin d^4, low-spin d^7, d^9) Jahn–Teller distortions are generally operative, giving rise to large distortions from octahedral symmetry, which quench the orbital momentum. In T-terms, on the other hand, SOC is generally sufficient to remove the degeneracy, but leaving a large unquenched orbital momentum. A useful example is high-spin cobalt(II) (d^7). In octahedral symmetry the ground state is $^4T_{1g}$. The orbital degeneracy is three-fold so the multiplet comprises 12 states, on the whole. The states are split by SOC to give a ground Kramers doublet, separated by ca. 100–150 K from the excited multiplets [2,23]. Low-symmetry components of the ligand field may slightly change this pattern, but in most cases a single Kramers doublet will be populated at low temperature. This can be treated as an effective $S = 1/2$ spin. In octahedral symmetry the isotropic g-value is around 4.33 due to the unquenched orbital contribution. In lower symmetries the g-values depend on the splitting of the d orbitals, and in a first approximation on that of the t_{2g} orbitals. Since these are π^* orbitals their splitting, and the sign of the magnetic anisotropy,

depends on the π interaction between metal and ligand orbitals. If the *xz*, *yz* orbitals lie lower than *xy*, $g_{\|}$ becomes smaller than $g = 4.33$, while $g_{\perp}$ slightly increases as shown in Fig. 1. The two sets of curves correspond to the strong- and weak-ligand field limit, respectively. The limit values for strong distortions are $g_{\|} = 2$, $g_{\perp} = 4$. This corresponds to an easy-plane type magnetic anisotropy, because the external field will tend to orient the spins in the *xy*-plane, where the highest *g*-values are observed. If the *xz*, *yz* orbitals lie higher than *xy* the limiting values become $g_{\|} = 8$–9, $g_{\perp} = 0$. In this case the magnetic anisotropy is of the easy-axis type, because the field will preferentially orient the spins parallel to *z*. The general problem of the *g*-values of high-spin cobalt(II) in low-symmetry environments has also been discussed [24].

Other configurations giving rise to *T*-type ground states are d^1, d^2, low-spin d^4, low-spin d^5, high-spin d^6 [25]. Quite often the d^1 configuration corresponds to M=O ions, in which the strong metal–oxygen bond strongly quenches the orbital contributions. All the other ions do give rise to sizeable *g*-anisotropy. Among these one can indicate low-spin iron(III) [26].

The metal ions of the second and third transition series have larger SOC constants. However they also show larger covalency which tends to give excited states at higher energies. Therefore they also show only moderate *g*-anisotropy.

The second contribution to the magnetic anisotropy comes from the zero-field splitting (ZFS). The term zero-field splitting refers to the fact that a given *S*-multiplet, which in spherical symmetry is degenerate in zero-field, has its degeneracy removed when the symmetry is lower. The asymmetry can be described by a series expansion in magnetic multipoles [27]. The first term is the quadrupolar one, which depends on the second power of the spin operators and can be observed for systems with $S \geq 1$. In a spin-Hamiltonian formalism it is described by:

$$\mathbf{H} = D[\mathbf{S}_z^2 - S(S+1)/3] + E(\mathbf{S}_x^2 - \mathbf{S}_y^2) \quad (2)$$

D is different from zero if the symmetry is lower than cubic, while *E* is only different from zero if the symmetry is lower than axial (*x* is different from *y*). The

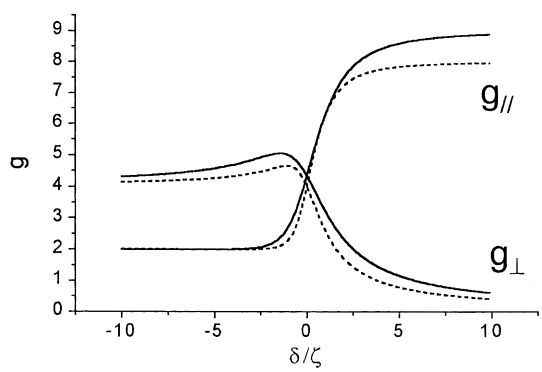

Fig. 1. Dependence of the *g*-values of high-spin cobalt(II) complexes on an axial distortion parameter δ. The solid curves correspond to the weak-field limit while the dashed curves to the strong-field limit.

first term is diagonal in the $|S,M\rangle$ basis, while the second admixes states which differ in M by ± 2.

The origin of the ZFS can be twofold. The first contribution is given by the direct interaction between the magnetic dipoles of the unpaired electrons, while the second is brought about by SOC. The former, which is dominant for organic radicals, is typically of the order of 0.01 cm^{-1}, therefore it gives a small anisotropy, which will be discussed in the next paragraph. The latter is dominant for transition-metal ions, and can be of the order of a few cm^{-1}.

The SOC contribution is the same which is responsible for the deviation of the g-values from the free-electron value. In order to predict the sign and the intensity of the ZFS a simplified formula [26] can be used which relates the D and E parameters to the g-values:

$$D = \frac{\lambda}{2}\left[g_z - \frac{g_x + g_y}{2}\right], \quad E = \frac{\lambda}{4}(g_x - g_y) \tag{3}$$

where λ is the SOC constant within a given Russell–Saunders multiplet. It is related to the SOC constant of the ion, ζ, by the relation $\lambda = \pm \zeta/2S$, where the '+' sign applies to configurations d^n with $1 \leq n \leq 4$ and the '−' sign to $6 \leq n \leq 9$. If $|\lambda|$ is large, as in ions with large n, large ZFS can be anticipated even for relatively small g-anisotropy [2]. For instance in a tetragonally elongated nickel(II), typical g-values are: $g_z = 2.30$, $g_x = g_y$ 2.25. Since $\zeta = 649$ cm^{-1} the corresponding D-parameter is -8.11 cm^{-1}. The negative sign of the ZFS parameter corresponds to an easy-axis type magnetic anisotropy.

The second term contributing to ZFS is the hexadecapolar one, which depends on the fourth power of the spin operators and can be observed for systems with spin $S \geq 2$. The most appropriate way to express the corresponding Hamiltonian is through the so-called Stevens operator equivalents [23]

$$\mathbf{H} = \sum_k B_4^k \mathbf{O}_4^k \tag{4}$$

where the $\mathbf{O}_k^4$s are linear combinations of spin operators raised to the fourth power and the B_4^k coefficients must be determined from experiment. The sum is extended to $k = 0$–4. The number of terms to be retained depends on the symmetry of the center: for tetragonal symmetry only $k = 0$ and 4 are needed, for trigonal symmetry only $k = 0$ and 3, while for orthorhombic symmetry only 0, 2 and 4 are different from zero. The origin of these terms is the higher-order admixture of excited states into the ground state via SOC.

The g, D, E and B_4^k parameters can be obtained from the comparison with experiment. However it is possible to calculate them with several techniques. It can be expected that in short it will be possible to calculate the spin-Hamiltonian parameters using ab initio approaches. So far however it is possible to use ligand-field theories, which can provide an acceptable insight into the magnetic anisotropy as shown in the above discussion. These treatments however in general stop at axial symmetry and do not yield much guidance for lower symmetries. Recently, Bencini et al. [28] have generated a computer code which can calculate the

spin-Hamiltonian parameters without any symmetry requirement. This can be an excellent tool for choosing suitable building blocks to introduce the required anisotropy in a molecular magnet.

2.2. Spin–spin anisotropy

When more than one magnetic center is present in a cluster other terms must be included to define the magnetic anisotropy. These can be described as spin–spin interactions, and originate from either through-space or through-bond interactions [29]. The former are given by the coupling between the magnetic centers through dipolar interactions. At the simplest level of approximation these can be calculated treating the magnetic centers as point dipoles. The approximation is valid if the distance between the dipoles is large compared to their extension.

Point-dipolar interactions between two systems characterized by spin S_1 and S_2, respectively, are easily calculated using the Hamiltonian:

$$\mathbf{H} = \mathbf{S}_1 \cdot \mathbf{D}_{12} \cdot \mathbf{S}_2 \tag{5}$$

where

$$\mathbf{D}_{12} = \mu_B^2 \frac{\mathbf{g}_1 \cdot \mathbf{g}_2 - 3(\mathbf{g}_1 \cdot \mathbf{R})(\mathbf{R} \cdot \mathbf{g}_2)}{R^3} \tag{6}$$

In Eq. (6), **R** is a unit vector parallel to the 1–2 direction and R the distance between the two magnetic centers. For a pair of spins the dipolar interaction tends to align them parallel to each other, giving rise to easy-axis type anisotropy, parallel to the line connecting the two centers. The magnitude of the dipolar terms scales as R^{-3}. For two spins $S = 1/2$ at 3 Å, characterized by isotropic $g = 2$, the splitting of the triplet state determined by the dipolar interaction is 0.096 cm^{-1}, with the ± 1 components lying lowest. This corresponds to easy-axis type anisotropy.

The through-bond interactions originate from the admixture of excited states into the ground state through SOC. There is no simple rule available to predict the sign and the magnitude of the anisotropy induced by this term. Extensive correlations have been attempted for copper(II) dinuclear species [29]. The anisotropic-exchange terms are expected to be small for centers with low SOC constants, such as the organic radicals, the S-type metal ions (high-spin Mn^{II}, Fe^{III}, Gd^{III}, etc.), and in general all the systems in which the g-values are close to the spin-only value.

2.3. Anisotropy of spin clusters

The anisotropy of a spin cluster will be given by the sum of all the contributions described above. In the case that the isotropic exchange is much larger than all the other interactions the total spin S is a good quantum number and the g, D, and higher-order terms for each S-multiplet can be expressed by projecting the individual spins on the total spin [29]:

$$\mathbf{g}_S = \sum_i c_i^S \mathbf{g}_i, \quad \mathbf{D}_S = \sum_i d_i^S \mathbf{D}_i + \sum_{i<j} d_{ij}^S \mathbf{D}_{ij} \tag{7}$$

where c_i^S, d_i^S and d_{ij}^S are coefficients which can be calculated when the individual, the intermediate and the total-spin values are defined. The validity of Eq. (7) has been verified several times. It is important to stress that Eq. (7) is a tensorial one, which means that the principal directions of the various tensors must be taken into account.

2.4. Molecular anisotropy and crystal anisotropy

The first important point to make is that all the magnetic anisotropy measurements performed on a single crystal provide information on the crystal anisotropy. The principal axes of the susceptibility tensor will reflect the space-group symmetry and will coincide with the unit-cell axes in the case of orthorhombic, trigonal, tetragonal and hexagonal lattices. In monoclinic space groups only the *b* axis is a symmetry axis, therefore one principal direction of the tensor must be parallel to it. In a triclinic space group no symmetry is present, beyond possibly inversion symmetry, therefore the principal magnetic axes are not simply related to crystal axes. The experimental measurement of magnetic anisotropy is therefore particularly difficult for triclinic lattices, because the susceptibility tensor must be reconstructed through many measurements, performing several rotations. In a monoclinic space-group (with *b* unique) it is sufficient to measure the susceptibility parallel to *b*, and then to explore the *ac*-plane. In the orthorhombic system three measurements are required parallel to *a*, *b*, and *c*, while in trigonal, tetragonal and hexagonal groups only two measurements are needed (parallel and perpendicular to the unique axis).

The measured crystal anisotropy does not in general correspond to the molecular anisotropy. However, quite often the two quantities coincide and this happens when the following two conditions are met. First, only one crystallographically independent molecule must be present in the lattice. Second, the molecular symmetry must not be lower than that required by the highest-order symmetry axis in the space group. For instance in a trigonal system, if the molecule has trigonal point-group symmetry the observed anisotropy is the molecular anisotropy (neglecting intermolecular interactions). If however the site symmetry is lower than trigonal, there will be three molecules differing in orientation, related by 120° rotations as shown in Fig. 2. If the molecule has an easy-axis type anisotropy the crystal anisotropy can range from easy-axis to easy-plane in nature, depending on the angle θ between the easy molecular axis and the trigonal axis. If $\theta = 0°$ (a) all the easy axes are parallel to each other and the crystal anisotropy is of the easy-axis type, while if $\theta = 90°$ (b) the crystal anisotropy is of the easy-plane type. The crystal can also be completely isotropic if θ takes the 'magic-angle' value $\theta = \arccos(3^{-1/2}) \cong 54.74°$. Therefore caution must always be exerted in interpreting the experimental data.

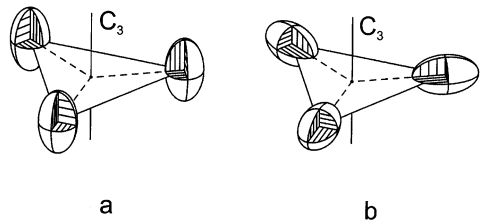

Fig. 2. Three symmetry-related anisotropic centers with individual anisotropy axis parallel (a) and perpendicular (b) to the unique crystal axis.

3. SQUID magnetometry

SQUID magnetometers are now widely used in many chemical laboratories. Their use for the measurement of the magnetic anisotropy is associated with their sensitivity, which allows one to use relatively small crystals. In this case the procedure for measuring the magnetic anisotropy is that of aligning different crystal axes with the applied magnetic field. Contrary to the torque methods to be described below, which measure the difference in magnetization in a given crystal plane, here the principal values of the magnetization are directly measured, with the limitations indicated in Section 2.4.

A beautiful recent example of the determination of anisotropic magnetic properties in molecular magnets has been provided by Kahn and co-workers [30]. $Mn_2(H_2O)_5Mo(CN)_7 \cdot 4H_2O$ has been obtained by assembling $[Mo(CN)_7]^{4-}$ and Mn^{2+} building blocks. The strategy was that of looking for other Prussian blue derivatives, which had been shown to yield room-temperature ferrimagnets [31,32]. Prussian blue derivatives are difficult to crystallize due to their poor solubility and consequent rapid precipitation. Therefore the authors decided to lower the symmetry of one of the building blocks by using the pentagonal bipyramidal $[Mo(CN)_7]^{4-}$ anion. $Mn_2(H_2O)_5Mo(CN)_7 \cdot 4H_2O$ crystallizes in the monoclinic space group $P2_1/c$, and crystals of size $4 \times 0.5 \times 0.2$ mm^3 could be investigated. The temperature dependence of the magnetization of a polycrystalline sample showed a transition to ferromagnetic order below $T_C = 51$ K. This is a quite respectable temperature for a molecule-based ferromagnet. Measurements on single crystals showed that *a*, *b*, and *c** are the principal directions of the magnetization tensor. Notice that *b* is required by symmetry to be a principal magnetic direction, the other two being in the *ac* plane. *a* and *c** were experimentally determined to correspond to the principal axes by rotating the crystal and selecting the orientations corresponding to the extreme of the magnetization. It was found that *b* is the easy magnetization axis in weak fields, *a* is the hard axis, and *c** is the intermediate axis as shown in Fig. 3. On increasing the field the magnetization parallel to *a* increases much more rapidly than that of other directions, and in a field of 0.2 T it becomes comparable to that parallel to *b*. This behavior is associated with a spin-canting process, which could only be observed through single-crystal measurements.

Another relevant application of magnetic anisotropy measurements has been performed with highly symmetric molecular clusters, which provided some evidence for the role of antisymmetric exchange in frustrated antiferromagnetic systems. $(NH_2Me_2)_{18}(NH_4)_6[(V^{IV}O(H_2O))_6(Mo(\mu\text{-}H_2O)_2(\mu\text{-}OH)Mo)_3(Mo_{15}(MoNO)_2O_{58}(H_2O)_2)_3] \cdot 14H_2O$, V_6, is a large cluster whose structure [33,34] is shown in Fig. 4. The molybdenum ions are essentially diamagnetic, therefore the magnetic properties are associated with the six oxovanadium(IV) ions embedded in the cluster [35].

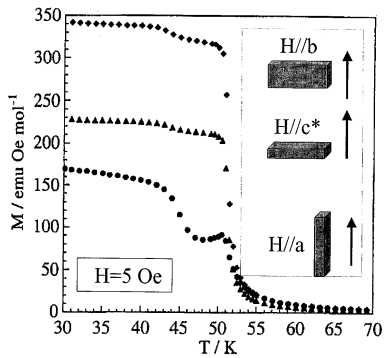

Fig. 3. Temperature dependence of the magnetization of $Mn_2(H_2O)_5Mo(CN)_7 \cdot 4H_2O$ along the *a*, *b* and *c** crystal axes.

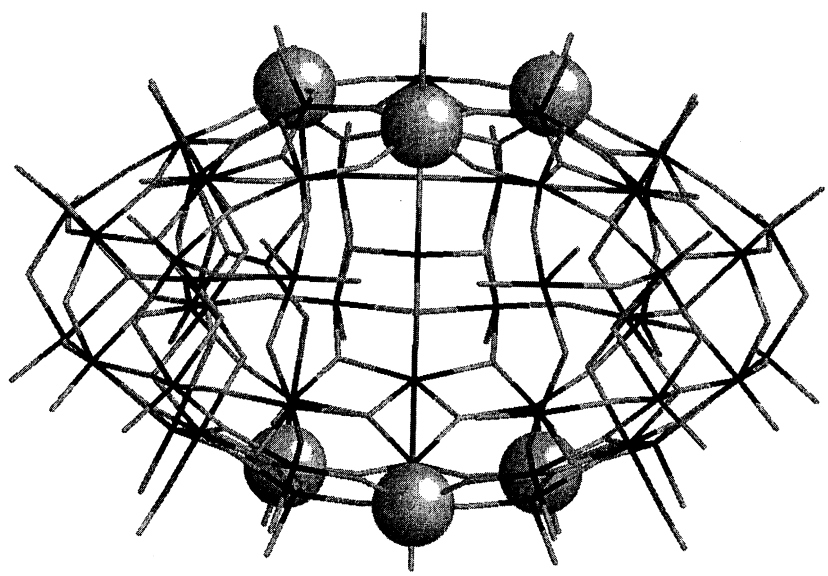

Fig. 4. View of the structure of the $[(V^{IV}O(H_2O))_6(Mo(\mu\text{-}H_2O)_2(\mu\text{-}OH)Mo_3(Mo_{15}(MoNO)_2\text{-}O_{58}(H_2O)_2)_3]^{24-}$ cluster. The vanadium ions are evidenced as large spheres. The molybdenum and oxygen atoms are represented by dark gray and pale gray rods, respectively.

They define a trigonal prism with metal–metal distances of 6.543 Å in the triangular faces and 9.587 Å in the vertical rectangular faces. The vanadium ions are bridged by molybdate groups. The V_6 clusters have trigonal symmetry, and so does the crystal (space-group $P6_3/mmc$). The temperature dependence of χT of a polycrystalline sample shows evidence of strong antiferromagnetic coupling within the triangles, which gives rise to a plateau, corresponding to ca. 0.7 emu mol^{-1} K in the 30–80 K range [36]. This value corresponds to two unpaired electrons localized on the two triangles. Below 20 K, χT decreases again and reaches 0.43 emu mol^{-1} K at 2.3 K. This seems to be evidence for anti-ferromagnetic coupling between the two triangles, even if the distance between the two triangles is very long. Attempts to fit the experimental magnetic susceptibility using two coupling constants, one within the triangle (J) and one between the triangles (J') yielded: $J = 158$, $J' = 3.3$ cm^{-1}, where J is defined by the Hamiltonian of isotropic exchange $H_{ex} = J\mathbf{S}_a\mathbf{S}_b$. However the fit was far from satisfactory at low temperatures. Now the important point which has so far been completely neglected is that equilateral triangles give rise to spin-frustration effects in the presence of antiferromagnetic exchange [37]. This means that the ground state is a pair of degenerate spin doublets. As in all cases of degeneracy the system will tend to remove it, either by lowering the symmetry (Jahn–Teller distortion) or through SOC. Since the coupling of the spin levels to the vibrations is weak the static distortion is not very probable, and the SOC mechanism (antisymmetric exchange) is presumably more favorable. The theory for this has long been known, and it predicts that one of the consequences of degeneracy lifting by SOC is a marked anisotropy [38]. In fact $\chi_{\|}$ is expected to remain unchanged, while $\chi_{\perp}$ is strongly affected at low field and low temperatures:

$$\chi_{\perp} = N_A g^2 \mu_B^2 \frac{\tanh\left(\frac{\sqrt{4G^2 + (g\mu_B B)^2}}{2k_B T}\right)}{\sqrt{4G^2 + (g\mu_B B)^2}} \tag{8}$$

where G is the parameter describing the antisymmetric exchange interaction (N_A is Avogadro's number). The temperature dependence of $\chi_{\|}T$ and $\chi_{\perp}T$ was measured on a single crystal, with the field parallel and perpendicular to the trigonal axis, respectively. The increase of the magnetic anisotropy on decreasing temperature allowed the determination of the value of $G = 9$ cm^{-1}. To our knowledge this is the best example of the experimental determination of antisymmetric exchange, and it was determined by the direct measurement of the magnetic anisotropy.

4. High-field torque magnetometry

4.1. Introduction

Torque magnetometry is a versatile macroscopic method for the characterization of magnetic substances in single-crystal form [4,5]. The technique itself has long been used in magnetochemistry, but the need for large crystals has hampered its

application to molecular compounds. The recent introduction of cantilever devices, to be briefly discussed in Section 4.2, has made it possible to use tiny single crystals thus making TM again palatable.

The TM technique measures the mechanical couple (**t**) experienced by a magnetic sample under the influence of a homogeneous magnetic field $\mathbf{B} = (B_x, B_y, B_z)$:

$$\mathbf{t} = \mathbf{M} \times \mathbf{B} \tag{9}$$

where $\mathbf{M} = (M_x, M_y, M_z)$ is the bulk magnetization. Without loss of generality we can assume that **M** and **B** lie in the xz-plane, so that the magnetic torque vector $\mathbf{t} = (t_x, t_y, t_z)$ is necessarily parallel to y (see Fig. 5). It follows that $t_x = t_z = 0$ while the y-component is given by:

$$t_y = M_z B_x - M_x B_z = B^2 \left(\frac{M_z}{B_z} - \frac{M_x}{B_x} \right) \sin\theta \cos\theta \tag{10}$$

where θ is the angle between the magnetic field and the z-axis. Hence, the experiment measures the anisotropy of the magnetization in the xz-plane. From Eq. (9) it follows that the origin of the magnetic torque is the non-collinearity between the applied magnetic field and the magnetization of the sample ($\theta \neq \varphi$), i.e. the presence of transverse magnetization components. The origin of the non-collinearity is different in permanent magnets and in paramagnets.

In the former, the magnetic moment is fixed with respect to the sample axes and its direction is simply determined by the crystal orientation. For instance, if the spontaneous magnetic moment is directed along the z-axis ($\varphi = 0$), the sample will tend to rotate counter-clockwise and eventually bring the magnetic moment along **B**. In this case, the term in parenthesis in Eq. (10) (hereafter referred to as axial anisotropy) reduces to M/B_z so that Eq. (10) becomes:

$$t_y = BM \sin\theta \tag{11}$$

where $B = |\mathbf{B}|$ and $M = |\mathbf{M}|$. Notice that the torque vanishes for $\theta = 0$ or 180°, and that the torque modulus is simply proportional to the bulk magnetization. Indeed, this approach has been recently used to measure magnetization in SMM below the blocking temperature [39,40].

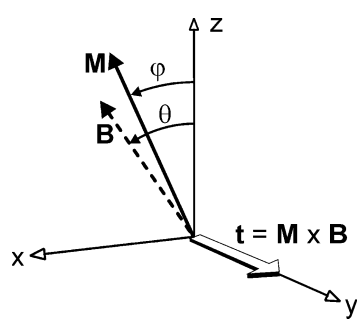

Fig. 5. Geometrical arrangement of the external field, **B**, of the sample magnetization, **M**, and of the torque vector, **t**, in a torque experiment.

In paramagnetic materials, on the other hand, the magnetic moment is field-induced and the transverse magnetization components are a direct consequence of paramagnetic anisotropy. In this case, TM represents a powerful tool for magnetic anisotropy investigations, as shown by the earlier applications of this technique to simple transition-metal complexes. The different approaches to be used for crystals belonging to the various crystal systems have been previously described [4,5]. Here we will not enter any detail, but work out a simple example. We assume an $S=1$ spin in axial symmetry, with isotropic $g=2.00$ and crystal-field parameters $D=-0.2\ \mathrm{cm}^{-1}$, $E=0$. The crystal-field induced anisotropy is of the easy-axis type, i.e. the magnetization at low temperature will preferentially orient along, say, z. The behavior of the system is different in the weak-field ($g\mu_B B \ll k_B T$) and in the strong-field ($g\mu_B \gg k_B T$) limits. In the former case, the magnetization is simply $\mathbf{M}=\chi\mathbf{B}=(\chi_{xx}B_x,\chi_{yy}B_y,\chi_{zz}B_z)$ so that if the field is rotated in the xz-plane the axial anisotropy is just the difference between the z- and x-magnetic susceptibilities, $\chi_{zz}-\chi_{xx}$. Consequently, the torque t_y at a fixed θ-angle is simply proportional to the square of the magnetic field:

$$t_y = B^2(\chi_{zz}-\chi_{xx})\sin\theta\cos\theta \tag{12}$$

Notice that the torque is zero when the magnetic field is applied along a principal direction ($\theta = n\pi/2$ with n integer),[1] and goes through extremes for $n\pi/4$. This simple relationship has been extensively used to determine the difference between principal susceptibilities in paramagnetic compounds [4,5].

The quadratic field-dependence of the torque breaks down completely in the high-field regime. In fact, when the magnetization reaches its saturation value for a system with isotropic g, such as the one we are considering, the axial anisotropy goes to zero. A quantitative treatment (see Appendix A), shows that the decrease of the axial anisotropy in a strong field follows a B^{-2}-law. This leads to an asymptotic behavior of the torque [41], which approaches the limiting value

$$\lim_{B\to\infty} t_y = -2DS(S-1/2)\sin\theta\cos\theta \tag{13}$$

In Fig. 6 we show the complete field dependence of the torque and of the axial anisotropy for the $S=1$ system defined above. The magnetic field is applied in the xz principal plane of the magnetization with $\theta=45°$ and $T=2.0$ K. A double logarithmic scale is used to enlighten the B^2-type dependence of the torque in low fields and the inverse square dependence of the axial anisotropy in high fields. Notice that the torque saturates to $0.1\ \mathrm{cm}^{-1}\ \mathrm{rad}^{-1}$, as predicted by Eq. (13) with $D=-0.2\ \mathrm{cm}^{-1}$, $S=1$ and $\theta=45°$. A similar scenario holds for a hard-axis paramagnet, with an opposite sign of D and t_y. The simple relationship in Eq. (13) is useful not only for isolated paramagnets, but also for exchange-coupled systems. For instance, it has been recently exploited to determine the pattern of D values in the excited states of anti-ferromagnetic clusters, as described in Section 4.3.

[1] This is a general result. In fact, the torque component along a generic α-axis can also be obtained by differentiating the magnetic energy, E_M, with respect to the angle, θ_α, which describes the rotation of the system around α at constant $\mathbf{B}$, i.e. $t_\alpha = -\mathrm{d}E/\mathrm{d}\theta_\alpha$. The derivative vanishes when the magnetic field is applied along a principal magnetic directions, leading to zero torque.

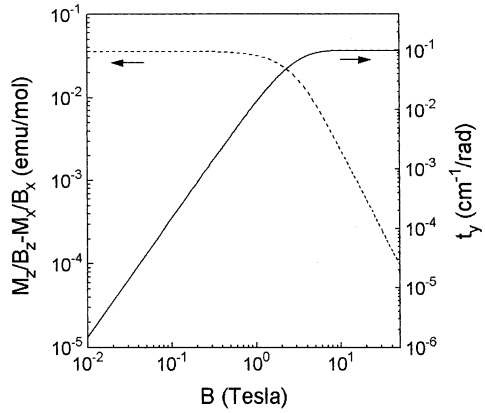

Fig. 6. Calculated field dependence of the torque component t_y and axial anisotropy of an $S = 1$ spin ($D = -0.2$ cm^{-1}, $E = 0$, $g = 2.00$, $\theta = 45°$, $T = 2.0$ K).

4.2. Torquemeters

In the earlier applications of TM, a single-crystal sample was simply suspended by a calibrated torsion wire (usually a quartz fiber) and the magnetic torque was measured by using the 'flip-angle' or 'null-deflection' methods. The measured torque directly provided the difference between the principal magnetic susceptibilities (Eq. (12)), from which the principal susceptibilities themselves could be determined with the aid of an average-susceptibility measurement [4,5]. The importance of this technique has increased greatly in recent years, following the development of new experimental devices with increased performance and sensitivity, specifically designed for small (often microscopic) samples. These include cantilever- [42–44] and rotor- (wheel) [45] torquemeters, the latter being inherently insensitive to mechanical noise due to their symmetrical design. The sample is anchored to the cantilever surface or to the rotatable platform. The magnetic torque is then translated into a small displacement of the mobile part of the device, which can be detected by various means, such as capacitive, piezoresistive, piezoelectric or optical techniques. Capacitive detection is particularly convenient due to the simple electronics required, which includes an AC bridge and a lock-in amplifier. A cantilever apparatus has the advantage of being a constructively simple device, as shown in Fig. 7. The cantilever is made of silicon or a non-magnetic metallic alloy (typically CuBe) and comprises a sample-hosting area and one or two thin legs. The cantilever is mounted parallel to a fixed metal platform to give a parallel-plate capacitor, whose capacitance C (neglecting edge effects) is given by:

$$C = \varepsilon \frac{A}{d} \tag{14}$$

A is the area of the plates, ε is a dielectric constant of the medium in which the torquemeter is operated and d is the separation between the two electrodes (usually

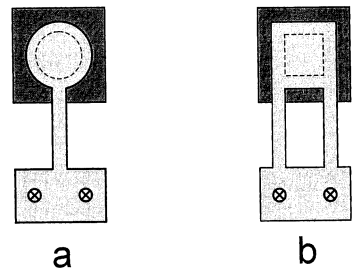

Fig. 7. Top-view of one-leg (a) and two-legs (b) cantilevers, depicted in light gray. The sample-hosting area is delimited by a dashed line. The lower plate of the torquemeter is in dark gray.

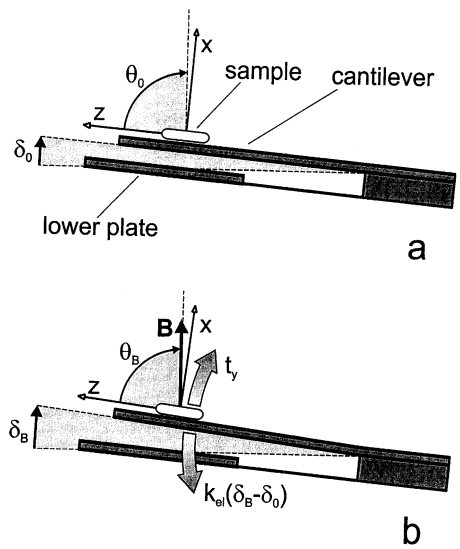

Fig. 8. Side-view of a typical experimental setup used in a CTM experiment. The cantilever deflection due to the applied magnetic field in (b) is exaggerated for the sake of clarity.

< 100 μm). In this case, the device is sensitive to the component of the torque vector which is responsible for cantilever flexion. However, two-legs piezoresistive silicon cantilevers which are sensitive to both flexion and torsion have been micro-fabricated to detect two components of the torque vector [43]. A typical experimental apparatus, which provides a practical realization of Fig. 5, is shown in Fig. 8a. The single crystal is mounted on the cantilever so that the yz-plane is parallel to the cantilever surface, while the setting angle $\theta_0 = 90 - \delta_0$ can be chosen by properly rotating the whole torquemeter around the y-axis. If the z-axis is an easy magnetic direction in the xz-plane, application of a magnetic field **B** leads to an increase of the δ-angle to a new equilibrium value δ_B, with a decrease in the capacitance (Fig. 8b). For small deflections, the difference between δ_B and δ_0 (torque instability) can be neglected, and the device approaches a linear-response

regime in which the capacitance variation is directly proportional to the magnetic torque t_y [46]:

$$\Delta C = C_B - C_0 \propto -t_y \tag{15}$$

It is apparent that exceedingly high sensitivities can be achieved through a suitable design of the capacitor, for instance by using soft springs and/or by reducing the separation between the electrodes. As a consequence, CTM works nicely even on very small single crystals (down to a few micrograms).[2] This feature has further expanded the applications of cantilever magnetometers, which can be used for magnetization measurements as well. In this case, one exploits either the force acting on the sample in a magnetic field gradient ('force mode') or the torque which tends to align a permanent magnetic moment along the applied field ('torque mode'). In this configuration, cantilever magnetometers can be easily made more sensitive than traditional SQUID-based methods.

Applications of TM in high magnetic fields and at very low temperatures have fully exploited the development of these miniaturized cantilever or wheel devices, which can be easily hosted in the restricted confines of ^{3}He/^{4}He cryostats or dilution refrigerators. Furthermore, the performances of these torquemeters are not affected by high magnetic fields. As a result, this technique has been widely used in solid-state physics, for instance for the characterization of High-T_c superconductors or magnetic thin films. Molecule-based magnetic materials have not been investigated in detail by this technique until recently, when high-field torque studies of large spin clusters have been reported. These are the subjects of the next two sections.

4.3. Spin crossover in antiferromagnetic clusters

CTM has been used to investigate the electronic structure of anti-ferromagnetic (AF) clusters which show field-tunable ground spin states [47]. The most thoroughly studied compounds of this class are ring-like iron(III) clusters comprising up to 18 metal centers [48–56]. These systems often exhibit high molecular symmetries, either crystallographically dictated or idealized. For instance, many Fe_6 rings crystallize in a trigonal space group and exhibit rigorous S_6 point-group symmetry (Fig. 9) [49–52], while two Fe_{10} clusters (often referred to as the 'ferric wheels') crystallize in monoclinic space groups but have idealized D_{5d} symmetry (Fig. 10) [53,54]. The former appear to be particularly well suited for anisotropic magnetization measurements, because the crystal anisotropy corresponds to the molecular anisotropy. In both cases, only one exchange-coupling constant $J > 0$ is required to describe AF Heisenberg interactions between nearest-neighboring metal centers, and the pattern of lowest-lying spins levels follows the simple expression:

[2] Capacitive torquemeters based on Cu/Be cantilevers can detect torques signals down to 10^{-12} N m. By using Eq. (12), this correspond to an axial anisotropy of 10^{-13} emu in a field of 1 T (recall that $T^2 = 10$ N m emu^{-1}).

$$E(S,M) = \frac{2J}{N} S(S+1) + g\mu_B MB \quad (16)$$

where B is an applied magnetic field and N is the number of spins in the ring. The relative magnitude of the exchange and Zeeman terms in the right-hand side of Eq. (16) dictates the S-value in the ground state. In the absence of a magnetic field ($B = 0$), the ground state of an even-membered ring is clearly non-magnetic ($S = 0$). However, magnetic spin states are progressively stabilized with increasing magnetic field, until eventually the ground state becomes magnetic at the critical field B_1 (see Fig. 11). Weak AF interactions are in general observed ($J = 10$–40 cm^{-1}), so that several iron(III) rings show the transition from $S = 0$ to $S = 1$ in moderate fields (< 20 T). In some cases, multiple crossovers can be induced in the experimentally accessible field range (B_1, B_2, B_3, etc.). At low temperature, each crossover is usually accompanied by an abrupt variation in the static magnetic properties, such as magnetization and magnetic torque. The spin dynamics is also dramatically affected by the (anti)crossing between spin levels, as demonstrated by the enhanced proton

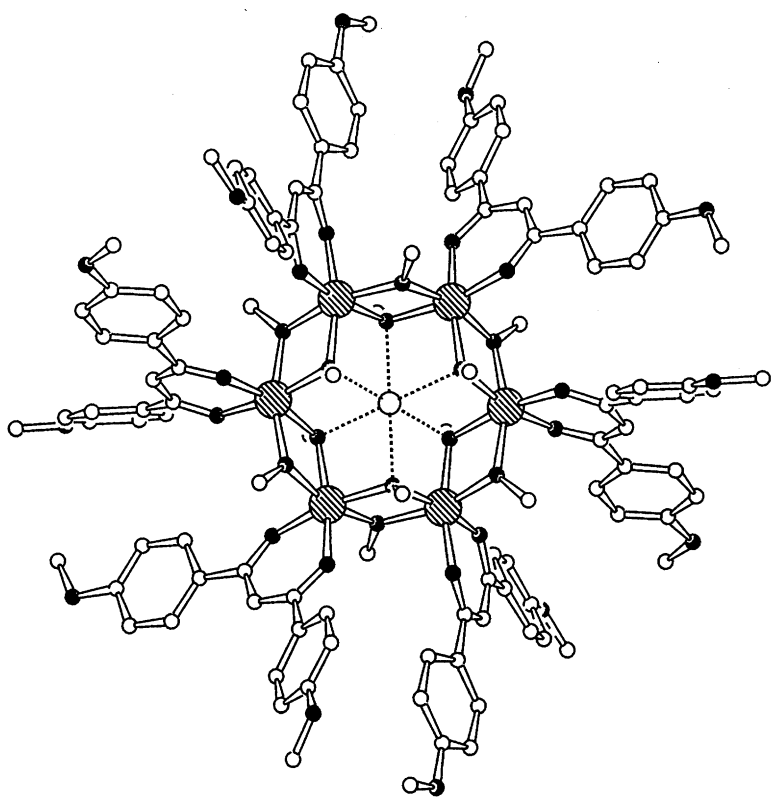

Fig. 9. Structure of $[NaFe_6(OCH_3)_{12}(pmdbm)_6]^+$, $NaFe_6$, (Hpmdbm = 1,3-bis(4-methoxyphenyl)-1,3-propanedione). Atom code: large hatched circles = Fe; large empty circle: Na; small empty circles = C; small black circles = O.

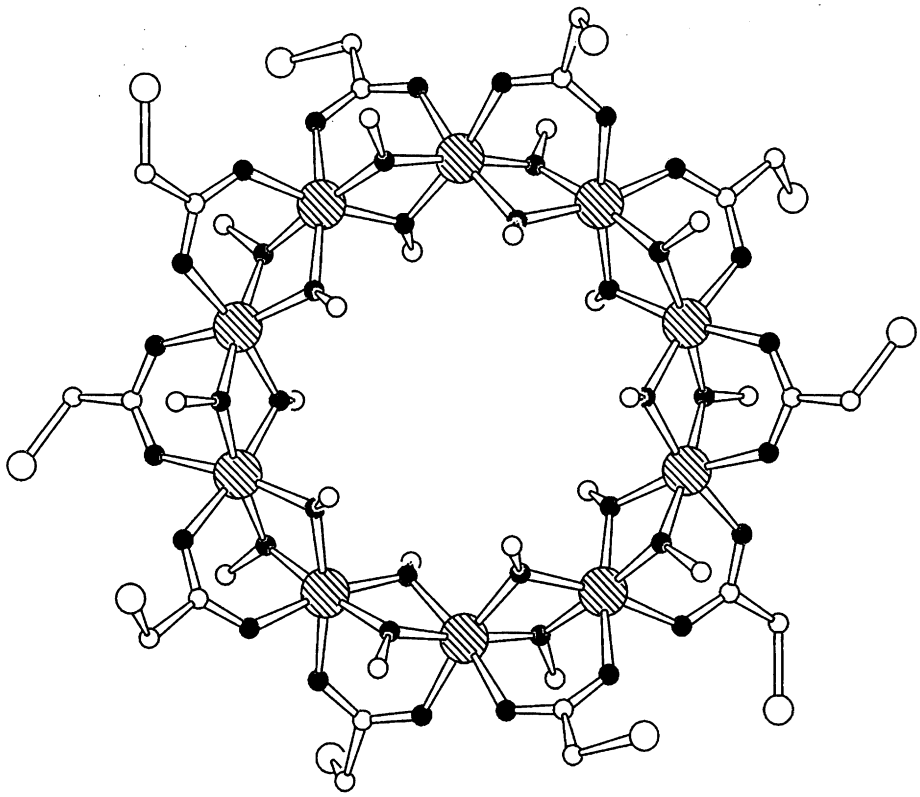

Fig. 10. Structure of $[Fe_{10}(OCH_3)_{20}(CH_2ClCO_2)_{10}]$, Fe_{10}. The atom code for Fe, O and C is the same as in Fig. 9. Large empty circles represent Cl atoms.

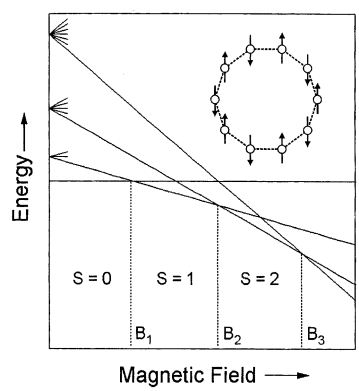

Fig. 11. Field dependence of the low-lying energy levels of an antiferromagnetic ring of ten $S = 5/2$ spins.

spin–lattice relaxation rate measured by solid-state NMR [57,58]. The detection of field-induced crossover by TM exploits the different magnetic anisotropy of the involved spin states [59–61]. In Fig. 12 we report torque curves recorded at different temperatures on a single crystal of $NaFe_6$ by applying the magnetic field at an angle $\theta = \pi/4$ from the six-fold cluster axis [60,61]. The step-like field dependence of the torque signal, which becomes more pronounced at lower temperature, reflects the large magnetic anisotropy of the $S = 1$ state when compared to the non-magnetic character of the $S = 0$ state. Additional steps are at higher fields ($\sim$ 32.6, 48.9 T, etc.). However, host–guest interactions provide an easy handle to tune the magnetism of Fe_6 rings at the synthetic level. In fact, the size of the guest alkali-metal ion has a large influence on the strength of exchange-coupling interactions in the ring. More precisely, the J constant is reduced by almost 30% by replacing sodium with lithium in the cluster core. This allows the observation of two torque steps in the experimentally accessible field range in $LiFe_6$ (0–30 T) [41]. Similarly, the smaller J-value and the larger number of spins in the Fe_{10} ring lead to five observable torque steps in the range 0–23 T [60,61].

Stepped torque curves can be used to investigate the electronic structure of antiferromagnetic clusters, as they provide information on exchange interactions and on the ZFS parameters, D_S, of the excited spin states. A very convenient approach developed in our laboratory is based on the observation that, for an anisotropic system, the level-crossing fields B_S depend on the θ-angle between the magnetic field and the unique molecular axis. More precisely, in the high-field regime ($g\mu_B B \gg D_S$) the magnetic field value required for the transition from S–1 to S is:

$$B_S(\theta) = \frac{\Delta_S + (\cos^2\theta - 1/3)A_S}{g\mu_B} \tag{17}$$

where A_S is a differential anisotropy parameter defined as

$$A_S = D_S S(S - (1/2)) - D_{S-1}(S - 1)(S - (3/2)) \tag{18}$$

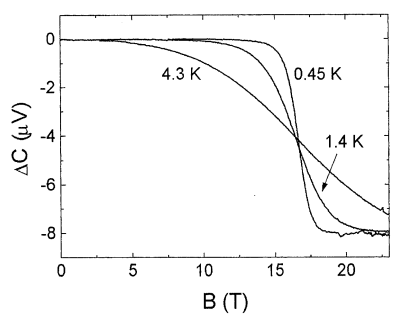

Fig. 12. Field dependence of magnetic torque acting on a single crystal of $NaFe_6$ at different temperatures.

and Δ_S is the energy gap between the $S-1$ and S multiplets at $B=0$. For instance, if we set $S=1$ and $D_0=0$, as appropriate for triplet–singlet crossing, B_1 ranges from

$$B_1(0) = (\Delta_1 + (1/3)D_1)/(g\mu_B) \tag{19a}$$

to

$$B_1(\pi/2) = (\Delta_1 - (1/6)D_1)/(g\mu_B) \tag{19b}$$

Level-crossing fields coincide with the inflection points of the torque steps and can be precisely determined at very low temperatures, where the steps become narrower. Although traditional magnetization measurements would in principle afford the same information [53,62], TM represents a more convenient technique especially in high magnetic fields and when high sensitivities are required. Indeed, the whole pattern of D_S-values can be determined either by extending the above-described procedure to successive level-crossings or by using Eq. (13). These procedures have been successfully applied to Fe_6 and Fe_{10} [41,60,61]. All these systems have positive D_S-values, so that the magnetic field value required, say, for singlet–triplet crossing is lower when the applied field lies in the ring plane. Notice that similar results can be obtained by electron paramagnetic resonance (EPR), as shown by a recent investigation on $[Fe_6(tea)_6]$ (H_3tea = triethanolamine) [63]. Nevertheless, TM appears to be of more general applicability. In fact, EPR may easily fail due to large ZFSs, excessive dipolar broadening or unfavorable spin–lattice relaxation rates at the temperatures required to populate the excited multiplets.

These results have contributed to understanding the origin of magnetic anisotropy in large magnetic clusters. Exchange anisotropy terms in polyiron(III) compounds are usually negligible due to the essentially isotropic g-tensor of the iron(III) ion. By contrast, dipolar interactions are found to contribute substantially to the observed easy-plane anisotropy. In fact, due to the dominant antiferromagnetic coupling, dipolar terms favor an arrangement of the spins perpendicular to the ring plane [64]. Indeed, magnetic anisotropy in $LiFe_6$ and Fe_{10} is almost entirely dipolar in origin [41,60,61]. On the other hand, large single-ion terms must be introduced in order to explain the anisotropy of $NaFe_6$ [41].

4.4. Magnetic anisotropy and quantum tunneling of the magnetization in high-spin molecules

The $Mn_{12}Ac$ cluster, $[Mn_{12}O_{12}(OAc)_{16}(H_2O)_4]\cdot 2AcOH\cdot 4H_2O$, has been the first high-spin molecular cluster exhibiting a hysteresis loop of purely molecular origin. The cluster has S_4 symmetry in the solid state and comprises four manganese(IV) ions ($S=3/2$) and eight manganese(III) ions ($S=2$) (Fig. 13). Since the crystal is tetragonal this is an ideal compound for measuring the magnetic anisotropy. The hierarchy of exchange-coupling interactions, which occur mainly through the μ_3-oxo ligands, results in a ferrimagnetic spin structure with an $S=10$ ground state. High-frequency EPR spectroscopy has shown that the ground $S=10$ manifold is largely split in zero applied field, with an axial zero-field splitting parameter, D, of

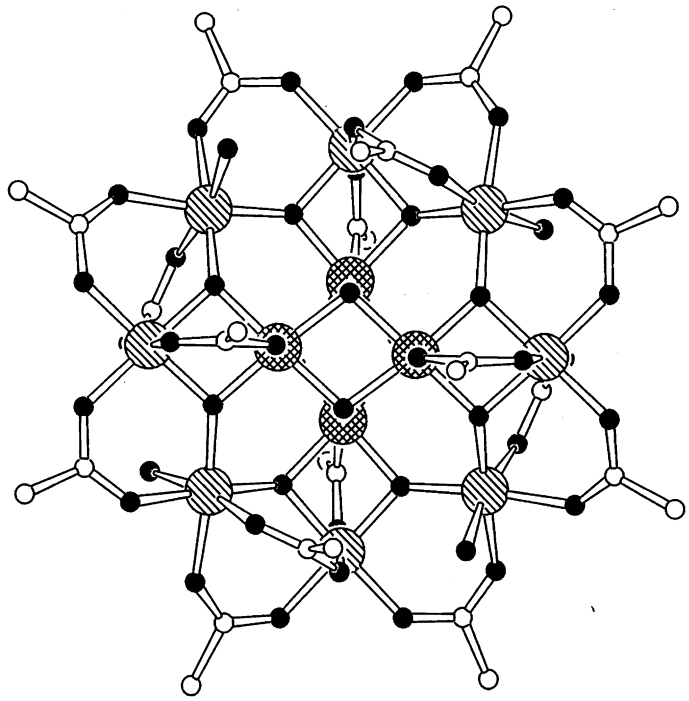

Fig. 13. Structure of $[Mn_{12}O_{12}(OAc)_{16}(H_2O)_4]$. The atom code for O and C is the same as in Fig. 9. Large hatched and gridded circles represent manganese(III) and manganese(IV), respectively.

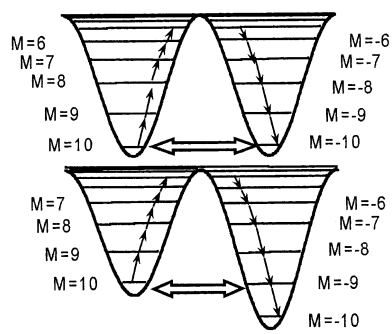

Fig. 14. View of the splitting of the $S = 10$ manifold in zero-field (top) and in a longitudinal field $H_z = |D|/g\mu_B$ where the $M = n$ and $M = -n + 1$ levels have the same energy (bottom).

the order of $-0.39\ cm^{-1}$ [65]. The $M = \pm 10$ states thus lie lowest in energy, as shown in Fig. 14, and the system exhibits a large magnetic anisotropy of the easy-axis type. The energy difference between the ground $M = \pm 10$ states and the $M = 0$ state is as large as $40\ cm^{-1}$ and, from a classical viewpoint, corresponds to the energy barrier to be overcome for the reversal of the magnetization. However,

at very low temperature the reversal of the magnetization occurs in a stepwise fashion as a function of magnetic field, with acceleration of the relaxation whenever the magnetic field has critical values that bring levels on the opposite sides of the barrier in energy coincidence as shown in the bottom of Fig. 14 for the levels $M = n$ and $M = -n + 1$. In these cases tunneling through the barrier is strongly enhanced and therefore the relaxation is faster thanks to what has been called a resonant quantum tunneling mechanism. To date, the magnetic properties of $Mn_{12}Ac$ have been investigated by TM following two different approaches. In the first approach, CTM was used to probe the magnetization reversal below 2.8 K [39,40]. In these conditions, the magnetic moment is essentially frozen along the easy ($\pm z$) direction, so that TM can be used to measure magnetization through Eq. (11). The magnetic field was applied very close to the z-axis ($\theta < 1°$) and the spin dynamics was studied in the field range 0–10 T. In the second approach, the torque method was used to evaluate the spin-Hamiltonian parameters associated with second-(D) and fourth-order (B_4^0) anisotropy terms [46][3]. Upfield and downfield torque curves were recorded at 4.2 K by applying the magnetic field (0–30 T) close to the hard (xy) magnetic plane of an $Mn_{12}Ac$ single crystal ($\theta = 90.0 \pm 1.1°$) (Fig. 15). Under these conditions non-hysteretic behavior is observed, consistently with a superparamagnetic regime. This result is expected since the temperature of the experiment, 4.2 K, is above the blocking temperature for quasi-static measurements. Moreover a strong transverse magnetic field can easily induce reversal of the magnetization. In the low-field region the torque signal is proportional to B^2, as predicted by Eq. (12). A pronounced peak is detected at ca. 6.2 T, while in high fields an asymptotic field dependence is observed (see Eq. (13)). The values $D = -0.468(7)\ cm^{-1}$ and $B_4^0 = -2.4(1) \times 10^{-5}\ cm^{-1}$ are found to provide the best fit with $g_{xx} = g_{yy} = 1.96$ and $g_{zz} = 1.93$.[3] The agreement with the same parameters determined by HF-EPR [65] and inelastic neutron scattering (INS) [66] experiments is remarkable.

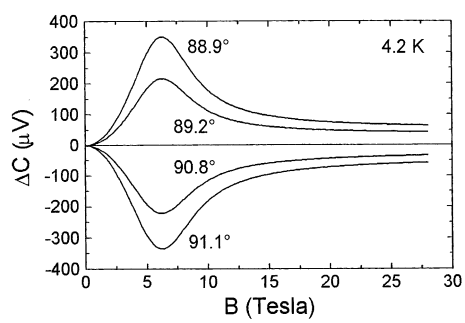

Fig. 15. Field dependence of the magnetic torque acting on a single crystal of $Mn_{12}Ac$ at 4.2 K. The angle θ between the external field and the easy axis of $Mn_{12}Ac$ is indicated.

[3] The spin-Hamiltonian parameters $\alpha = -0.389(5)$ and $\beta = -8.4 \times 10\ cm^{-1}$ used in Ref. [46] are related to D and B_4^0 through the equations $\alpha = D - [30S(S+1) - 25]B_4^0$ and $\beta = 35\ B_4^0$.

5. Micro-SQUID arrays

The μ-SQUID technique is very similar to the traditional SQUID technique. The essential difference is that the pick-up coil is replaced by a direct coupling of the sample with the SQUID loop. When a small sample is directly placed on the wire of the SQUID loop, the sensitivity of the μ-SQUID technique is nine orders of magnitude better than for a traditional SQUID. This result is only achieved when the size of the sample is smaller than that of the SQUID.

A magnetometer can be constructed using planar micro-bridge DC superconducting quantum interference devices (SQUID) fabricated by standard electron-beam lithography [67]. The SQUID consists of a square loop, about 1–2 μm wide and interrupted by two micro-bridge Josephson junctions. The dimensions of the SQUID arms are between 0.05 and 0.4 μm, as shown in Fig. 16. The SQUID loops can be fabricated with Al or Nb: the former is operational up to the temperature of 1 K (the superconducting critical temperature of Al), while with the latter 7 K can be achieved. The first instrument was developed in the 'Centre de Recherche des Tres Basses Temperature', CNRS, Grenoble [68]. An improved version at the L. Néel laboratory, CNRS Grenoble, has been used for the investigation of the magnetic properties of molecular clusters.

The sample is positioned through a piezo-electric quartz. If the sample is very close to a SQUID the response will be sensitive to the local environment, while if the sample is removed farther, then the response will be mediated over the entire sample. The high sensitivity of the techniques allows the measurement of single crystals of 10–500 μm. The magnetometer at L. Néel laboratory works now in fields up to 1.4 T, but an upgrading to 5 T is in course.

An early application was the measurement of the magnetization of cobalt clusters deposited using low-energy cluster beam techniques. The clusters were directly deposited over the chips, and the average size of the particles ranged from 2 to 6 nm [69].

Another interesting feature of the magnetometer is that the field can be swept at very high speed. In fact the sweeping rate can be as high as 30 T s^{-1}. Also the field stability is very high, better than 10 μT s^{-1}. Finally the time resolution is also high, about 1 ms, allowing short-time measurements.

All these unique features have been recently exploited in the analysis of the dynamics of the magnetization of large magnetic clusters. This technique has been

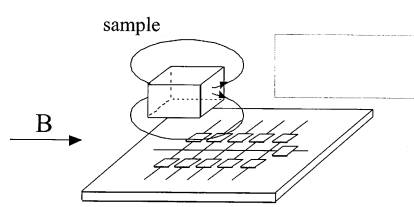

Fig. 16. Schematic view of the μ-SQUIDs' array used to measure the magnetization of samples placed in direct contact with the SQUID loops.

used in order to characterize a defective species present in $Mn_{12}Ac$, the cluster mentioned in Section 4.4 [70]. The defective species, which is present in concentrations of 1–2%, has a tunneling relaxation much faster than the major species. The measurements of the low-temperature magnetization are therefore easier for the former, because it is not necessary to wait for years, as is the case for the latter. Both the major and the minor species are characterized by a stepped hysteresis, which is due to thermally assisted quantum tunneling. The stepped hysteresis of the minor species can be easily measured with the μ-SQUIDs' array between 40 mK and 1.0 K, as shown in Fig. 17, because the magnetization of the major species is completely frozen at these temperatures and fields. By cooling the sample in zero-field the major species is non-magnetized and therefore does not affect the measurements. The steps observed in Fig. 17 correspond to the fields at which the tunneling is enhanced by the degeneracy of pairs of M levels. The steps occur at fields almost regularly spaced by 0.39 T. This period is sensibly smaller than that observed in the major species [16] and suggests a smaller D-value, $D = \Delta B/g\mu_B = -0.42\,cm^{-1}$ The hysteresis curve becomes practically independent of temperature below 600 mK. This seems to be a good evidence for quantum tunneling between the lowest $M = \pm 10$ levels. No such evidence could be achieved for the major species, due to its extremely long relaxation times in this temperature range. Matters are different for the minor species, which has been revealed to have a lower barrier for the reorientation of the magnetization and faster relaxation.

Another advantage of the μ-SQUIDs' magnetometer is the possibility of applying the magnetic field along any direction and controlling separately the three components of the magnetic field. Due to the reduced dimensions of the device, the arrays of SQUIDs loops can be located inside three orthogonal miniaturized superconducting solenoids. The measurements on the minor phases of $Mn_{12}Ac$ as a function of the orientation of the field suggest that the easy axis is not collinear with that of the major species, the crystallographic c-axis, and therefore the minor species lacks the four-fold symmetry. The faster tunnel relaxation observed for the minor species seems therefore to be originated by the lower symmetry of the magnetic anisotropy which induces a larger admixing of the M states on the opposite site of the barrier.

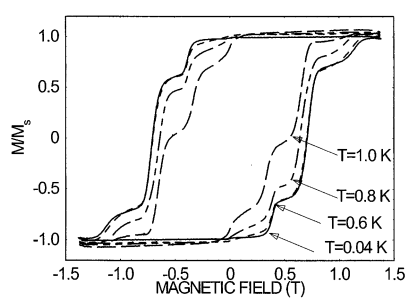

Fig. 17. Stepped hysteresis of the minor species of $Mn_{12}Ac$, measured at several temperatures. The magnetization is reported as a fraction of the saturation value. The major species does not contribute as its magnetization is frozen in a non-magnetic state by zero-field cooling.

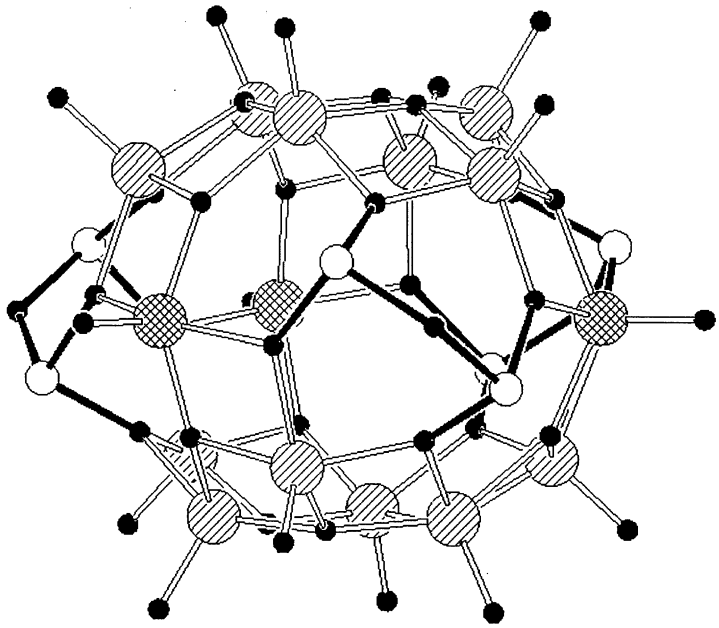

Fig. 18. Structure of the $[V^{IV}_{15}As_6O_{42}(H_2O)]^{6-}$. The vanadium ions are represented by large hatched circles. The three ions responsible of the low-temperature magnetism are evidenced by cross-hatching. Arsenic and oxygen are represented by empty and full circles, respectively.

By comparing the signal of different SQUIDs, placed close to the edges of the crystals or close to the center of the crystal, we concluded that the major species is homogeneously distributed in the crystal and not located on the surface, in agreement with the observation of isomeric forms in similar clusters containing a different carboxylic acid [71]. This possibility of performing a sort of magnetic imaging is one of the advantages of the μ-SQUID technique.

Another molecular cluster which was investigated with this technique is $K_6[V^{IV}_{15}As_6O_{42}(H_2O)] \cdot 8H_2O$, V_{15}, which comprises 15 oxovanadium(IV) ions, each with $S = 1/2$ [72]. The vanadium ions are grouped in three layers, two external ones with six metal ions, and a middle layer with three metal ions (Fig. 18). The external hexagons are strongly antiferromagnetically coupled in such a way that they are essentially non-magnetic at relatively high temperatures. The coupling between the three oxovanadinm(IV) ions of the internal layer is much weaker, giving a ground doublet-of-spin-doublets separated from the first excited quartet by ca. 3 cm^{-1}. This is a very interesting spin topology, which gives rise to spin frustration [73], as discussed in Section 3.

Recently, a small single crystal (~ 50 μm) of V_{15} was investigated with the μ-SQUID technique (50–400 mK, 0–0.7 T s^{-1}). The observed hysteresis loops, are due to slow relaxation but not originated by the presence of an energy barrier, as in the case of SMMs [74]. The phenomenon of hysteresis has been attributed to the

presence of a relatively large splitting of the ground doublet-of-doublets, which makes spin-phonon interactions responsible of the relaxation. The phonon bath is not in equilibrium with the temperature bath and therefore a time dependent magnetization is observed.

The μ-SQUIDs' magnetometer has also been used to investigate the dynamics of the magnetization of another SMM, namely $[Fe_8O_2(OH)_6(tacn)_6]Br_8 \cdot 9H_2O$, Fe_8 [75], whose structure is shown in Fig. 19. This cluster has a ground $S = 10$ spin state as $Mn_{12}Ac$ but has a smaller magnetic anisotropy [76]. The main difference is however the lower symmetry of Fe_8 compared to $Mn_{12}Ac$. In fact Fe_8 has a strong transverse magnetic anisotropy. The larger admixing of the $\pm M$ states makes this cluster the ideal system to investigate the quantum effects on the dynamics of the magnetization. In particular the direct tunnel transition between the almost degenerate $M = \pm 10$ states is observed below ca. 0.4 K [77]. A stepped hysteresis is observed, similar to $Mn_{12}Ac$, when the field is applied along the easy axis. As in the μ-SQUIDs' magnetometer the three components of the magnetic field can be controlled separately, it has been possible to observe the effects of a static magnetic field applied in the hard plane when sweeping the field component along the easy axis. It has then been observed that if the transverse field is applied along the intermediate axis the tunneling rate, which is proportional to the splitting of the ± 10 states, increases monotonically as intuitively expected, but oscillates when the field is closer to the hard axis [19]. The observed tunnel splitting as a function of the

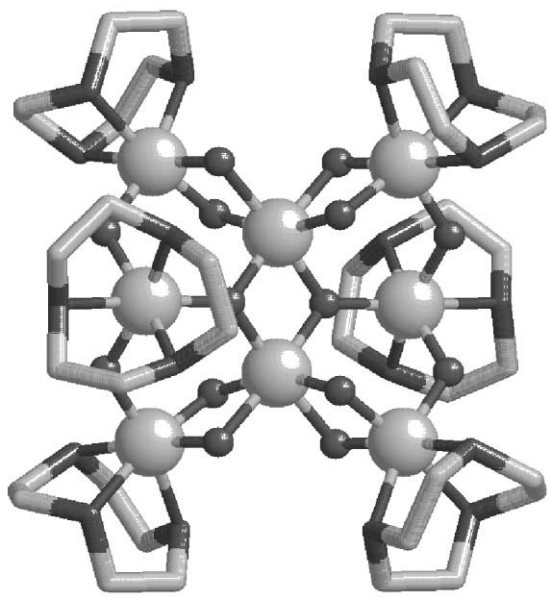

Fig. 19. View of the structure of the $[Fe_8O_2(OH)_6(tacn)_6]^{8+}$ cluster. The iron atoms are depicted as large spheres and the oxygen atoms as small dark spheres. The tacn (tacn = triazacyclononane) ligand is represented by sticks with the nitrogen atoms in dark gray.

applied field in the hard plane, at different angles from the hard axis, is shown in Fig. 20. Such behavior has been long predicted in a magnetic system but never observed before. It has been attributed to destructive interference of two tunneling pathways as observed in superconducting rings [78]. The hysteresis loop recorded sweeping the field along the easy axis, z, can be therefore modified by the application of a field along the hard axis, x, with some jumps of the magnetization strongly enhanced or reduced for critical values of the transverse field, as shown in Fig. 21. Which jumps are enhanced and which ones are reduced depend on the parity of the tunnel transition, that means if $M-M'$ is odd or even, when M and M' are the states on the opposite sides of the barrier involved in the tunneling process (see Fig. 14). In fact odd and even transitions present a similar oscillatory behavior of the tunneling rate but with a phase shift, as can be seen in Fig. 22.

These results potentially have technological interest. In fact in magnetic data storage a higher density of storage can be achieved by reducing the memory units, but the dimensions of the particles approach the superparamagnetic limit and thermal fluctuations of the magnetization reduce the stability of the data. A larger stability can be achieved by using harder magnetic materials with a larger

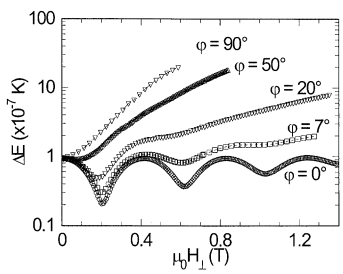

Fig. 20. Transverse field dependence of the tunneling splitting between the $M=10$ and $M=-10$ states of the ground $S=10$ multiplet of Fe_8 measured ad different angles from the hard axis, this last one corresponding to $\varphi=0°$.

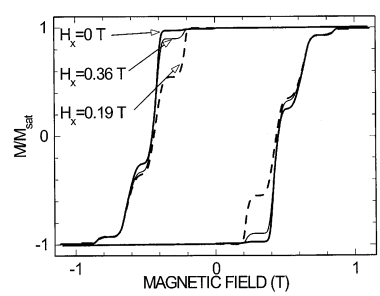

Fig. 21. Hysteresis loops observed for Fe_8 by sweeping the field along the easy axis and applying an addition field H_x along the hard axis. The jumps at ± 0.2 T are strongly enhanced for $H_x=0.19$ T while those at ± 0.4 T are reduced. The application of a field $H_x=0.36$ T gives a curve very similar to that obtained for $H_x=0$.

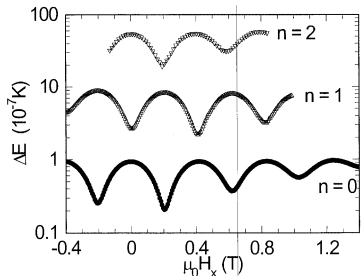

Fig. 22. Transverse field dependence of the tunneling splitting between the $M = 10$ and $M = -10 + n$ states of the ground $S = 10$ multiplet of Fe_8. The oscillations for n odd and even have opposite phase.

coercivity. However in this case a stronger magnetic field produced by the recording head is required in the writing process, thus providing another technological challenge. Among the possible solutions is that of 'softening' the area to be written for instance by heating it. In SMMs, where the reversal of the magnetization occurs through a tunneling process, the coercivity can be controlled through an application of a transverse field. This important observation has been possible through the use of a non-standard technique of magnetometry based on μ-SQUIDs' arrays.

6. Conclusions

Traditional magnetochemistry has rapidly evolved in the last few years, using techniques which at the beginning were in the realm of physics, and then have become more and more familiar to chemists. At the beginning room temperature measurements were performed, then the frontier moved to 77 K, then to 4.2 K. Now conventional magnetometers can go down to 1.8 K, pumping helium, and in many cases ^{3}He, and ^{3}He/^{4}He dilution refrigerators are used to reach the mK region. A similar escalation has been observed in the use of magnetic fields. Nowadays it is more and more common to perform measurements in high fields, up to 20 T and beyond. Pulsed experiments allow one to reach 40–50 T and in some limiting experiments, 800 T can be achieved. This trend of increasing sophistication is expected to continue, because the objects which are synthesized in the chemical laboratories continue to increase in complexity, and thus require more complex characterization techniques. Magnetism is a very difficult field, and experiments on single crystals are more and more desirable. Given the difficulty to grow large single crystals, inherent in the molecular nature of the compounds, it will be necessary to increase the sensitivity of the instrumentation. This will be needed also for studying nanostructured materials, which are being prepared at an increased rate. Molecular clusters have provided an important simplification to investigate nanoparticles, because since they are all identical to one other it has been possible to study large assemblies of them. However if they are to become really important also for technological reasons it will be necessary to address the individual molecules,

suitably arranged in ordered arrays. This will be the next frontier in molecular magnetism, that of the magnetic investigation of individual molecules.

Finally it must be remembered that the progress in the synthetic techniques and in the experimental tools to investigate the magnetic properties requires the parallel development of the theoretical models to interpret them. Also in this field the developments of the last few years have been fantastic, with the possibility of calculating the isotropic interaction between magnetic centers in an incredibly accurate way. The next steps will be in the calculations of larger and larger clusters, taking into account also the magnetic anisotropy starting from first principles.

Acknowledgements

The financial support of MURST is gratefully acknowledged as well as the collaboration of A.G.M. Jansen from the Grenoble High Magnetic Field Laboratory (MPI-FKF and CNRS, Grenoble, France) and W. Wernsdorfer from the Laboratoire Louis Neel (CNRS-Grenoble, France).

Appendix A. Limiting value of the torque for classical and quantum spins

Classical spins. We consider a classical spin $\mathbf{S} = (S \sin\varphi, 0, S\cos\varphi)$ under the competing effects of a magnetic field $\mathbf{B} = (B \sin\theta, 0, B\cos\theta)$ and a uniaxial anisotropy DS_z^2 (refer to Fig. 5, replacing **M** with **S**). The magnetic energy, E_M, and the axial anisotropy are given by

$$E_M = DS_z^2 - \mathbf{B}\cdot\mathbf{S} = DS^2\cos^2\varphi - BS\cos(\theta-\varphi) \tag{A1}$$

$$\frac{S_z}{B_z} - \frac{S_x}{B_x} = \frac{S\sin(\theta-\varphi)}{B\sin\theta\cos\theta} \tag{A2}$$

The equilibrium condition for the spin ($\partial E_M/\partial\varphi = 0$) is described by the equation:

$$\sin\varphi\cos\varphi = -\frac{B}{2DS}\sin(\theta-\varphi) \tag{A3}$$

Combining the last two equations and noticing that for $B\to\infty$ the spin is progressively oriented along the magnetic field direction ($\varphi\to\theta$), the axial anisotropy in high fields is:

$$\frac{S_z}{B_z} - \frac{S_x}{B_x} = -\frac{2DS^2}{B^2}\frac{\sin\varphi\cos\varphi}{\sin\theta\cos\theta} \cong -\frac{2DS^2}{B^2} \tag{A4}$$

so that the torque becomes field-independent:

$$t_y \cong -2DS^2\sin\theta\cos\theta \tag{A5}$$

Quantum spins. For a quantum spin with no g-anisotropy and axial ZFS, the high-field limiting value of t_y can be easily worked out by using first-order

perturbation theory. To perform the calculation, it is convenient to apply the magnetic field along the z-axis of the cartesian coordinate frame, while varying the angle, θ, between z and the anisotropy axis. The spin-Hamiltonian then takes the following form:

$$\mathbf{H} = \tfrac{1}{3}D[(2 - 3\cos^2\theta)\mathbf{S}_x^2 - \mathbf{S}_y^2 + (3\cos^2\theta - 1)\mathbf{S}_z^2 - 3\sin\theta\cos\theta(\mathbf{S}_x\mathbf{S}_z + \mathbf{S}_z\mathbf{S}_x)] + \mu_B g B\mathbf{S}_z \quad \text{(A6)}$$

Notice that the ZFS term reduces to the familiar expression $D[\mathbf{S}_z^2 - \frac{1}{3}S(S+1)]$ at $\theta = 0$. In the high-field regime ($g\mu_B B \gg k_B T$), the $|S, -S\rangle$ state is the only appreciably populated. Recalling that:

$$\langle S, -S|\mathbf{S}_x^2|S, -S\rangle = \langle S, -S|\mathbf{S}_y^2|S, -S\rangle = \tfrac{1}{2}S$$

$$\langle S, -S|\mathbf{S}_z^2|S, -S\rangle = S^2$$

$$\langle S, -S|\mathbf{S}_x|S, -S\rangle = \langle S, -S|\mathbf{S}_y|S, -S\rangle = 0$$

the first-order correction to the energy of the $|S, -S\rangle$ state is:

$$\langle S, -S|\mathbf{H}|S, -S\rangle = -\mu_B g B S + DS(S - (1/2))(\cos^2\theta - (1/3)) \quad \text{(A7)}$$

The y-component of the torque vector can be obtained by simply differentiating Eq. (A7) with respect to θ:

$$t_y = -2D_S S(S - (1/2))\sin\theta\cos\theta \quad \text{(A8)}$$

which coincides with Eq. (13).

References

[1] R.D.L. Carlin, Magnetochemistry, Springer, Berlin, 1986.
[2] J.S. Griffith, The Theory of Transition Metal Ions, Cambridge University Press, Cambridge, 1961.
[3] B. Bleaney, K.D. Bowers, Proc. R. Soc. A 214 (1952) 451.
[4] W. De. W. Horrocks Jr., D. De. W. Hall, Coord. Chem. Rev. 6 (1971) 147.
[5] S. Mitra, Prog. Inorg. Chem. 22 (1977) 309.
[6] R.D. Willett, D. Gatteschi, O. Kahn, Magneto-Structural Correlations in Exchange Coupled Systems, vol. C140, Reidel, Dordrecht, 1985 (pp. 207–240).
[7] O. Kahn, Molecular Magnetism, VCH, Weinheim, 1993.
[8] O. Kahn, Magnetism: a Supramolecular Function, vol. C148, Kluwer, Dordrecht, 1996.
[9] J. Veciana, J.J. Novoa, M. Deumal, J. Cirujeda, P.M. Lahti, Magnetic Properties of Organic Materials, Marcel Dekker, New York, 1999 (p. 573).
[10] D. Gatteschi, O. Kahn, J.S. Miller, F. Palacio, Magnetic Molecular Materials, vol. E198, Kluwer, Dordrecht, 1999.
[11] C.J. O'Connor, Prog. Inorg. Chem. 29 (1982) 203.
[12] R.L. Carlin, A.J. van Duyneveldt, Magnetic Properties of Transition Metal Compounds, Springer, Berlin, 1977.
[13] R. Morrish, The Physical Principles of Magnetism, Wiley, New York, 1966.
[14] R. Sessoli, D. Gatteschi, A. Caneschi, M.A. Novak, Nature 365 (1993) 141.
[15] D. Gatteschi, A. Caneschi, L. Pardi, R. Sessoli, Science 265 (1994) 1054.
[16] L. Thomas, F. Lionti, R. Ballou, D. Gatteschi, R. Sessoli, B. Barbara, Nature 383 (1996) 145.
[17] J.R. Friedman, M.P. Sarachik, J. Tejada, R. Ziolo, Phys. Rev. Lett. 76 (1996) 3830.

[18] A. Caneschi, T. Ohm, C. Paulsen, D. Rovai, C. Sangregorio, R. Sessoli, Magn. Magn. Mater. 177 (1998) 1330.
[19] W. Wernsdorfer, R. Sessoli, Science 284 (1999) 133.
[20] G. Aromi, S.M.J. Aubin, M.A. Bolcar, G. Christou, H.J. Eppley, K. Folting, D.N. Hendrickson, J.C. Huffman, R.C. Squire, H.L. Tsai, S. Wang, M.W. Wemple, Polyhedron 17 (1998) 3005.
[21] S.M.J. Aubin, Z.M. Sun, I.A. Guzei, A.L. Rheingold, G. Christou, D.N. Hendrickson, Chem. Commun. (1997) 2239.
[22] M. Kinoshita, Jpn. J. Appl. Phys. 33 (1994) 5718.
[23] A. Abragam, The Principles of Nuclear Magnetism, Clarendon, Oxford, 1961.
[24] L. Banci, A. Bencini, C. Benelli, D. Gatteschi, C. Zanchini, Struct. Bonding 52 (1982) 37.
[25] A.B.P. Lever, Inorganic Electronic Spectroscopy, Elsevier, Amsterdam, 1984.
[26] B.R. McGarvey, Transition Metal Chemistry, vol. 3, Marcel Dekker, New York, 1966 (p. 89).
[27] A. Bencini, D. Gatteschi, Transition Met. Chem. (1982) 8.
[28] A. Bencini, I. Ciofini, M.G. Uytterhoeven, Inorg. Chim. Acta 274 (1998) 90.
[29] A. Bencini, D. Gatteschi, EPR of Exchange Coupled Systems, Springer, Berlin, 1990.
[30] J. Larionova, R. Clerac, J. Sanchiz, O. Kahn, S. Golhen, L. Ouahab, J. Am. Chem. Soc. 120 (1998) 13088.
[31] S. Ferlay, T. Mallah, R. Ouahes, P. Veillet, M. Verdaguer, Inorg. Chem. 38 (1999) 229.
[32] S.M. Holmes, G.S. Girolami, J. Am. Chem. Soc. 121 (1999) 5593.
[33] A. Müller, E. Krickemeyer, S. Dillinger, H. Bögge, W. Plass, A. Proust, L. Dloczick, C. Menke, J. Meyer, R. Rohlfing, Z. Anorg. Allg. Chem. 620 (1994) 599.
[34] A. Müller, W. Plass, E. Krickemeyer, S. Dillinger, H. Bögge, A. Armatage, A. Proust, C. Beugholt, U. Bergmann, Angew. Chem. Int. Ed. Engl. 33 (1994) 849.
[35] A. Müller, F. Peters, M.T. Pope, D. Gatteschi, Chem. Rev. 98 (1998) 239.
[36] D. Gatteschi, R. Sessoli, W. Plass, A. Müller, E. Krickemeyer, J. Meyer, D. Soelter, P. Adler, Inorg. Chem. 35 (1996) 1926.
[37] J. Vannimenous, G. Toulouse, J. Phys. C 10 (1977) 537.
[38] B.S. Tsukerblat, M.I. Belinski, V.E. Fainzil'berg, Soviet Chem. Rev. 9 (1989) 337.
[39] J.A.A.J. Perenboom, J.S. Brooks, S. Hill, T. Hathaway, N.S. Dalal, Phys. Rev. B 58 (1998) 330.
[40] J.A.A.J. Perenboom, J.S. Brooks, S. Hill, T. Hathaway, N.S. Dalal, Physica B 246–247 (1998) 294.
[41] A. Cornia, M. Affronte, A.G.M. Jansen, G.L. Abbati, D. Gatteschi, Angew. Chem. Int. Ed. Engl. 38 (1999) 2264.
[42] M.J. Naughton, J.P. Ulmet, A. Narjis, S. Askenazy, M.V. Chaparala, A.P. Hope, Rev. Sci. Instrum. 68 (1997) 4061.
[43] J. Brugger, M. Despont, C. Rossel, H. Rothuizen, P. Vettiger, M. Willemin, Sens. Actuators 73 (1999) 235.
[44] M. Willemin, C. Rossel, J. Brugger, M.H. Despont, H. Rothuizen, P. Vettiger, J. Hofer, H. Keller, J. Appl. Phys. 83 (1998) 1163.
[45] S.A.J. Wiegers, A.S. van Steenbergen, M.E. Jeuken, M. Bravin, P.E. Wolf, G. Remenyi, J.A.A.J. Perenboom, J.C. Maan, Rev. Sci. Instrum. 69 (1998) 2369.
[46] A. Cornia, M. Affronte, A.G.M. Jansen, D. Gatteschi, A. Caneschi, R. Sessoli, Chem. Phys. Lett. 322 (2000) 477.
[47] A. Caneschi, D. Gatteschi, C. Sangregorio, R. Sessoli, L. Sorace, A. Cornia, M.A. Novak, C. Paulsen, W. Wernsdorfer, J. Magn. Magn. Mater. 200 (1999) 182.
[48] S.P. Watton, P. Fuhrmann, L.E. Pence, A. Caneschi, A. Cornia, G.L. Abbati, S.J. Lippard, Angew. Chem. Int. Ed. Engl. 36 (1997) 2774.
[49] A. Caneschi, A. Cornia, S.J. Lippard, Angew. Chem. Int. Ed. Engl. 34 (1995) 467.
[50] A. Caneschi, A. Cornia, A.C. Fabretti, S. Foner, D. Gatteschi, R. Grandi, L. Schenetti, Chem. Eur. J. 2 (1996) 1379.
[51] G.L. Abbati, A. Caneschi, A. Cornia, A.C. Fabretti, D. Gatteschi, W. Malavasi, L. Schenetti, Inorg. Chem. 36 (1997) 6443.
[52] R.W. Saalfrank, I. Bernt, E. Uller, F. Hampel, Angew. Chem. Int. Ed. Engl. 109 (1997) 2596.
[53] K.L. Taft, C.D. Delfs, G.C. Papaefthymiou, S. Foner, D. Gatteschi, S.J. Lippard, J. Am. Chem. Soc. 116 (1994) 821.

[54] C. Benelli, S. Parsons, G.A. Solan, R.E.P. Winpenny, Angew. Chem. Int. Ed. Engl. 35 (1996) 1825.
[55] G.L. Abbati, A. Caneschi, A. Cornia, A.C. Fabretti, D. Gatteschi, Inorg. Chim. Acta 297 (2000) 291.
[56] A. Caneschi, A. Cornia, A.C. Fabretti, D. Gatteschi, Angew. Chem. Int. Ed. Engl. 38 (1999) 1295.
[57] M.-H. Julien, Z.H. Jang, A. Lascialfari, F. Borsa, M. Horvatic, A. Caneschi, D. Gatteschi, Phys. Rev. Lett. 83 (1999) 227.
[58] A. Cornia, A. Fort, M.G. Pini, A. Rettori, Europhys. Lett. 50 (2000) 88.
[59] O. Waldmann, J. Schülein, R. Koch, P. Müller, H.P. Andres, H.U. Güdel, P. Allenspach, Inorg. Chem. 38 (1999) 5879.
[60] A. Cornia, A.G.M. Jansen, M. Affronte, Phys. Rev. B. 60 (1999) 12177.
[61] A. Cornia, A.G.M. Jansen, M. Affronte, Mol. Cryst. Liq. Cryst. 335 (1999) 1113.
[62] Y. Shapira, M.T. Liu, S. Foner, C.E. Dubé, P.J. Bonitatebus Jr., Phys. Rev. B. 59 (1999) 1046.
[63] B. Pilawa, R. Desquiotz, M.T. Kelemen, M. Weickenmeier, A. Geisselman, J. Magn. Magn. Mater. 177 (1998) 748.
[64] D. Gatteschi, R. Sessoli, A. Cornia, Chem. Commun. (2000) 725.
[65] A.L. Barra, D. Gatteschi, R. Sessoli, Phys. Rev. B 56 (1997) 8192.
[66] I. Mirebeau, M. Hennion, H. Casalta, H. Andres, H.U. Güdel, A.V. Irodova, A. Caneschi, Phys. Rev. Lett. 83 (1999) 628.
[67] D. Mailly, C. Chapelier, A. Benoit, Phys. Rev. Lett. 70 (1993) 2020.
[68] W. Wernsdorfer, PhD Thesis, Joseph Fourier University, Grenoble, France, 1996.
[69] W. Wernsdorfer, K. Hasselbach, A. Benoit, B. Barbara, D. Mailly, J. Tuaillon, J.P. Perez, V. Dupuis, J.P. Dupin, G. Guiraud, A. Perez, J. Appl. Phys. 78 (1995) 7192.
[70] W. Wernsdorfer, R. Sessoli, D. Gatteschi, Europhys. Lett. 47 (1999) 254.
[71] Z.M. Sun, D. Ruiz, E. Rumberger, C.D. Incarvito, K. Folting, A.L. Rheingold, G. Christou, D.N. Hendrickson, Inorg. Chem. 37 (1998) 4758.
[72] A. Müller, J. Döring, Angew. Chem. Int. Ed. Engl. 27 (1988) 1721.
[73] D. Gatteschi, L. Pardi, A.-L. Barra, A. Müller, J. Döring, Nature 354 (1991) 463.
[74] I. Chiorescu, W. Wernsdorfer, A. Müller, H. Bögge, B. Barbara, Phys. Rev. Lett. 84 (2000) 3454.
[75] K. Wieghardt, K. Pohl, I. Jibril, G. Huttner, Angew. Chem. Int. Ed. Engl. 23 (1984) 77.
[76] A.L. Barra, P. Debrunner, D. Gatteschi, Ch.E. Schulz, R. Sessoli, Europhys. Lett. 35 (1996) 133.
[77] C. Sangregorio, T. Ohm, C. Paulsen, R. Sessoli, D. Gatteschi, Phys. Rev. Lett. 78 (1997) 4645.
[78] A. Garg, Europhys. Lett. 22 (1993) 205.